Pergamon

Geochimica et Cosmochimica Acta, Vol. 67, No. 10, pp. 1889–1900, 2003

0016-7037/03 $30.00 + .00

doi:10.1016/S0016-7037(02)01285-1

Non-Henry's Law behavior of REE partitioning between fluorapatite and CaF_2-rich melts: Controls of intrinsic vacancies and implications for natural apatites

YUANMING PAN,[1,*] PING DONG,[1] and NING CHEN[1,2]

[1]Department of Geological Sciences, University of Saskatchewan, Saskatoon, SK S7N 5E2, Canada
[2]Canadian Light Source, University of Saskatchewan, Saskatoon, SK S7N 2C6, Canada

(*Received July* 19, 2002; *accepted in revised form October* 9, 2002)

Abstract—The partitioning of rare-earth elements (REEs: Gd and multiple REEs), Sr, and Mn between fluorapatite and CaF_2-rich melts was investigated over a wide range of REE concentrations (i.e., from 0.8 ± 0.1 to 25,000 ± 2600 ppm Gd in fluorapatite) in two different sample assemblies (i.e., tightly covered Pt crucibles and sealed Pt capsules) at 1220 °C and atmospheric pressure. Attainment of equilibrium is indicated by selected reversal experiments. The partition coefficient D(Gd) decreases from ~2 to ~0.5 with increasing Gd in fluorapatite, hence a marked non-Henry's Law behavior, but becomes independent of composition at and above ~5000 and ~1000 ppm Gd for experiments in Pt crucibles and Pt capsules, respectively. Non-Henry's Law behavior is also observed in experiments involving multiple REEs. All REE patterns are convex upward in shape with maxima between Nd and Gd, and D(La)/D(Nd) and D(Nd)/D(Yb) decrease systematically with increasing total REEs in fluorapatite, suggesting that REE fractionations are partly related to non-Henry's Law behavior. These experimental results and local structural data from previous electron paramagnetic resonance spectroscopic studies suggest that the non-Henry's Law behavior of REE partitioning between fluorapatite and melt is controlled by intrinsic Ca^{2+} vacancies in the c-axis channels. The D(Sr) and D(Mn) values are independent of composition and, therefore, do not deviate from the Henry's Law in their respective compositional ranges investigated in this study.

Nonstoichiometry, such as Ca^{2+} and F^- vacancies in the c-axis channels, is well known in natural apatites, particularly in biogenic apatites. Therefore, the observed non-Henry's Law behavior of REE partitioning is expected to have important implications for REE geochemical modeling involving apatites and for the uptake of REEs by natural apatites. Particularly, the non-Henry's Law behavior of REE partitioning is at least partly responsible for the commonly observed, bell-shaped REE patterns in fossil biogenic apatites. *Copyright © 2003 Elsevier Science Ltd*

1. INTRODUCTION

Henry's Law, which states that the activity (α) and concentration (X) of infinitely dilute species (i) are linearly related ($\alpha_i = K_iX_i$, where K_i is known as the Henry's Law constant), is of great importance in geochemistry. For example, one fundamental assumption made in trace element geochemical modeling for the origin and evolution of magmas is that the distribution of trace elements between coexisting minerals and melts/fluids obeys Henry's Law. However, laboratory experiments and analyses of natural samples have shown that the partition coefficients of some trace elements between several minerals and melts/fluids vary with the concentrations of these elements in the minerals, hence a non-Henry's Law behavior commonly known as "The Henry's Law Problem" (e.g., Mysen, 1978; Navrotsky, 1978; Siemann and Schramm, 2002). Several previous studies suggested that this non-Henry's Law behavior is controlled by various defect equilibria (Mysen, 1978; Navrotsky, 1978; Harrison and Wood, 1980). For example, Navrotsky (1978) classified the structural defects into (1) point defects (i.e., intrinsic vacancies, intrinsic interstitials, vacancy-hole combinations, altervalent substitutions producing vacancies or interstitials, partially filled sublattices) and (2) extended defects (i.e., linear, planar and 3-dimensional defects such as surface sites, edge dislocations, screw dislocations, shear planes, intergrowths of structure elements) and proposed that the non-Henry's Law behavior of trace element partitioning between minerals and melts might be related to metastable equilibria involving these structural defects. However, direct structural investigation of trace elements and associated defects within the concentration range where non-Henry's Law behavior is commonly observed has not been possible because of the lack of appropriate techniques in the past for structural characterization of extremely dilute species in solids.

Apatite-group minerals, particularly fluorapatite, are among the most important carriers of rare-earth elements (REEs) in igneous, metamorphic, and sedimentary rocks and in biomass as well (Pan and Fleet, 2002 and references therein). Numerous previous experimental studies have investigated the partitioning of REEs between apatite and melt/fluid (e.g., Watson and Green, 1981; Ayers and Watson, 1993; Fleet and Pan, 1997; Fleet et al., 2000a, 2000b; Harlov et al., 2002). These experimental studies have provided quantitative data about the controls of both intrinsic (crystal-chemical) and external (pressure-temperature-composition) factors on the uptake of REEs by apatite-group minerals (for review, see Pan and Fleet, 2002). However, almost all of these experimental studies were performed on REE-rich apatite, well above the concentration range where non-Henry's Law behavior was observed for other minerals (e.g., Mysen, 1978). Not surprisingly, non-Henry's Law behavior of REE partitioning between apatite and melt/fluid has

* Author to whom correspondence should be addressed (yuanming.pan@usask.ca).

Table 1. Summary of experimental conditions.

Series	REEs in starting materials	Sample assembly	Run condition/duration	Ref.
AP30	0 ppm Gd* to ~1 wt.% Gd_2O_3	tightly covered Pt crucible	1375°C for 24 h 1375°C to 1220°C at 2°C/h	1,2,3,4,5
AP40	~5 ppm Gd to ~15 wt.% Gd_2O_3	sealed Pt capsules	1375°C for 24 h 1375°C to 1220°C at 2°C/h 1220°C for 24 h	1,5
AP50	~5 to ~5000 ppm total REEs	sealed Pt capsules	1375°C for 24 h 1375°C to 1220°C at 2°C/h 1220°C for 24 h	1
AP60	~100 to ~10,000 ppm Gd	sealed Pt capsules	1220°C for 3 weeks	1

References 1, 2, 3, 4 and 5 are this study, Chen et al. (2002a), Chen et al. (2002b), Pan et al. (2002a), and Pan et al. (2002b), respectively. *Gd_2O_3 was not added to run AP30-0 but apparently came as a result of contamination from previous Gd-rich experiments that might have left trace amounts of Gd in either the Pt crucible or the furnace chamber (Pan et al., 2002a).

not been documented (e.g., Watson and Green, 1981). Recently, we conducted several synthesis experiments for the formation of Gd-doped fluorapatite from CaF_2-rich melts for single-crystal electron paramagnetic resonance (EPR) spectroscopic studies and single-crystal X-ray structure refinements (Chen et al., 2002a, 2002b; Pan et al., 2002a, 2002b). The EPR studies provided the first direct evidence for the involvement of intrinsic Ca^{2+} vacancies in the incorporation of Gd^{3+} ions into this mineral and noted an anomalous site preference of Gd over the two Ca sites at low concentrations (Chen et al., 2002b; Pan et al., 2002b). Accordingly, the experimental study was expanded to cover a wide range of Gd concentrations and to include other REEs to investigate possible non-Henry's Law behavior of REE partitioning between fluorapatite and CaF_2-rich melts.

The main objective of the present study is, therefore, to present new experimental results to demonstrate that there is a pronounced non-Henry's Law behavior of REE partitioning between fluorapatite and CaF_2-rich melts over a considerable range of REE concentrations. In addition, these new experimental results are integrated with crystal-chemical data (Chen et al., 2002a, 2002b; Pan et al., 2002a, 2002b) to show that the observed non-Henry's Law behavior is controlled by intrinsic Ca^{2+} vacancies. Moreover, the possible effects of the non-Henry's Law behavior of REE partitioning to the uptake of REEs by natural fluorapatite, particularly biogenic apatite, are discussed.

2. EXPERIMENTAL AND ANALYTICAL PROCEDURES

2.1. Synthesis Experiments

Four series of experiments (AP30, AP40, AP50, and AP60) were conducted (Table 1). The series AP30 experiments performed in a tightly covered Pt crucible (Prener, 1967) were originally designed to produce millimeter-sized fluorapatite crystals for EPR studies (Chen et al., 2002a, 2002b). Starting materials consisted of high-purity (≥ 99.99%) chemicals, including CaO from the British Drug House (BDH) or CaO obtained from decomposition of $CaCO_3$ from the Sigma-Aldrich Chemical Company (SACC) at 900 °C, and P_2O_5, CaF_2, and Gd_2O_3 from SACC. These chemicals were weighed after annealing at 500 °C for 24 h and mixed thoroughly by grinding in a porcelain mortar for ~6 h to form the composition of the ideal fluorapatite with varying amounts of Gd_2O_3. These mixtures (27.5 g), together with flux materials (22.5-g CaF_2), were placed in 50-mL Pt crucibles. The syntheses were carried out under atmospheric pressure in a Thermolyne 46100 Muffle Furnace equipped with a programmable controller at the Department of Geological Sciences, University of Saskatchewan (U of SK). The mixtures were first heated to 1375 °C (i.e., ~50 °C above liquidus; Prener, 1967) and held there for 24 h to ensure complete melting and homogenization and were then cooled down to 1220 °C at the rate of 2 °C/h and quenched in water. The experimental products invariably consisted of fluorapatite crystals and quenched phosphate-bearing CaF_2-rich glasses. The CaF_2-rich glasses, which were partly recovered for chemical analyses by drilling, were removed by boiling in an aqueous 20% solution of $Al(NO_3)_3 \cdot 9H_2O$.

The series AP40 experiments used similar starting materials to series AP30 but were made in sealed Pt capsules. A trial experiment of this series (AP40-0, ~15 wt.% Gd_2O_3 in the starting material) was made to produce fluorapatite crystals for an X-ray structure refinement (Pan et al., 2002b). The remaining series AP40 experiments were made from two mixtures: FAP-Gd containing ~20,000 ppm Gd and FAP-0 without any REEs. The experimental charges (~100-mg each) were prepared from FAP-Gd by sequential dilution using FAP-0 and were sealed in Pt capsules by welding. All Pt capsules were weighed before and after being placed in a 110 °C oven for 24 h to detect any leakage. The synthesis procedures of these experiments were similar to those of series AP30, except that series AP40 was held at 1220 °C for 24 h. All Pt capsules were weighed again after experiments to ensure no leakage. The experimental products of fluorapatite crystals and CaF_2-rich glasses were either separated by handpicking under a binocular microscope or sectioned and polished directly in Pt capsules for in situ chemical analysis (e.g., Fig. 1a,b).

The series AP50 experiments were similar in both sample assembly and run conditions to series AP40 (Table 1) but included 8 or 10 rare-earth oxides (La_2O_3 from BDH; Nd_2O_3 and Sm_2O_3 from Alfa Aesar; and Eu_2O_3, Gd_2O_3, Dy_2O_3, Ho_2O_3, Er_2O_3, Tm_2O_3, and Yb_2O_3 from SACC) mixed in approximately equal amounts by weight. This exclusive use of rare-earth oxides in the starting materials was based on the findings of Fleet and Pan (1995, 1997) who noted that the use of non-oxides (e.g., CeF_3 and $PrCl_3 \cdot 6H_2O$) resulted in anomalous partition coefficients from neighboring REEs with oxide dopants, owing to different substitution mechanisms (cf.

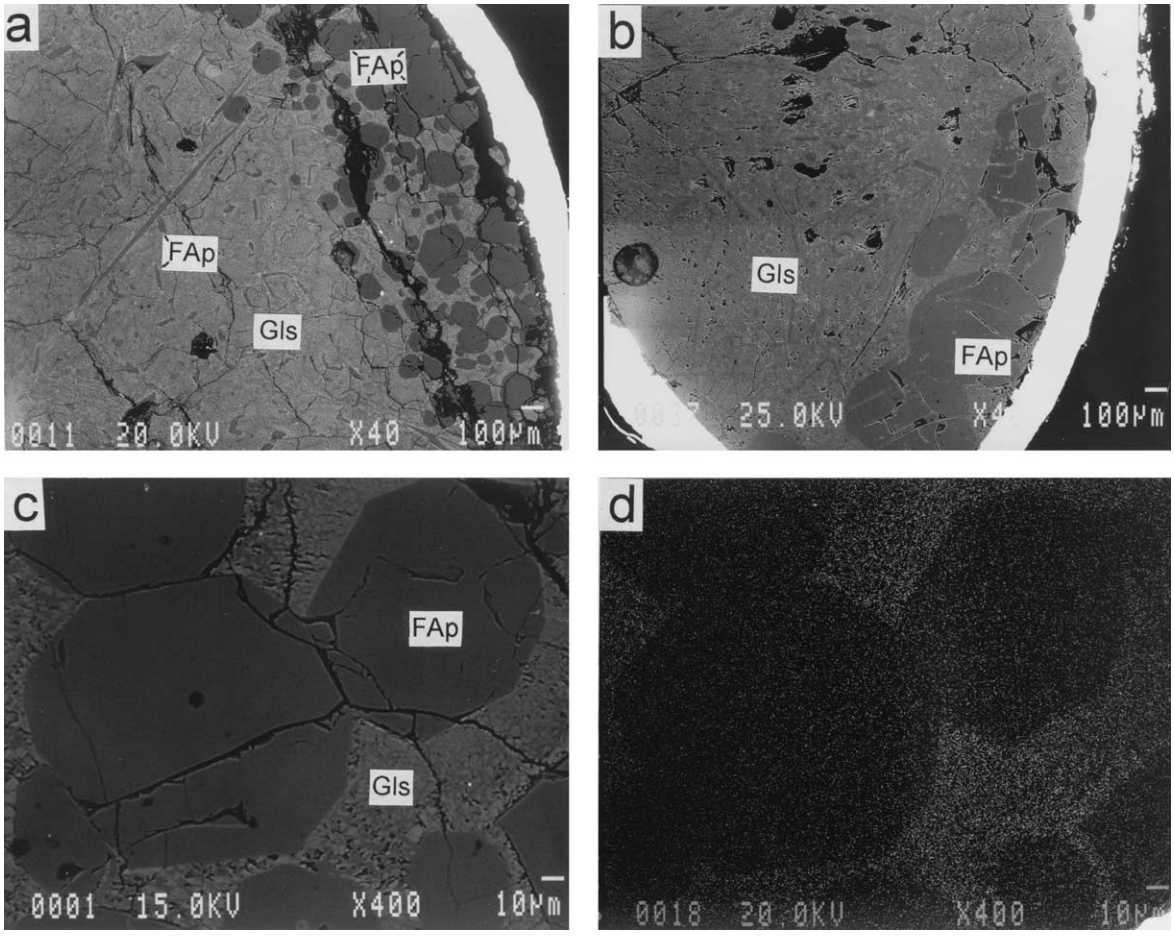

Fig. 1. Backscattered electron images (a, b, and c) and X-ray map (d) illustrating the experimental products of (a) cross-section of AP40-8 showing that fluorapatite crystals (FAp: dark gray) mostly lie at the bottom of Pt capsule; note that fluorapatite also occurs in the CaF_2-rich glass (Gls: light gray); (b) cross-section of AP60-2 showing fluorapatite crystals at the bottom of Pt capsule and in CaF_2-rich glass; (c) close-up of fluorapatite crystals without any evidence of compositional zoning in CaF_2-rich glass (AP40-8); and (d) homogeneous distribution of Gd in fluorapatite crystals and CaF_2-rich glass (AP40-8: same view as c). Note that Gd in fluorapatite crystals is notably lower than that in the CaF_2-rich glass (D(Gd) = 0.53; Table 4).

Mackie and Young, 1973; Chen et al., 2002a). Also, Ce_2O_3 was not included, because it is readily oxidized to CeO_2 in the presence of O_2 at the temperature range of this study. AP50-1, AP50-2, and AP50-3, containing eight REEs, were prepared from a mixture containing ~4000 ppm total REEs (i.e., ~500 ppm for each REE) by sequential dilution using FAP-0. AP50-4 was prepared separately to include 10 REEs and contained approximately ~20,000 ppm total REEs (i.e., ~2000 ppm for each REE) in the starting material. The experimental products were separated by handpicking under a binocular microscope.

The series AP60 comprised four experiments in sealed Pt capsules and was designed to test whether or not equilibrium was attained. Experiment AP60-1 used a mixture of fluorapatite crystals from the run products of experiment AP30-1 and CaF_2 from SACC in a weight ratio of 11 : 9. Experiments AP60-2, AP60-3, and AP60-4 used starting materials similar to those of experiments AP40-8, AP40-2, and AP40-4, respectively. These experiments were heated directly to 1220 °C, held there for 3 weeks, and then quenched in water. The products of these four experiments were all sectioned and polished in Pt capsules for in situ chemical analysis.

2.2. Analytical Procedures

All experimental products were first examined by optical microscopy. Selected crystals of fluorapatite and some of the separated CaF_2-rich glasses from series AP30 experiments were also investigated by Fourier-transform infrared (FTIR) absorption spectroscopy on a BIO-RAD FTS-40 spectrometer, using KBr pellets at the Departments of Chemistry, and by powder X-ray diffraction (XRD) analysis on a Rigaku Rotaflex X-ray diffractometer, using Ni-filtered CuKα radiation at the Department of Geological Sciences. Also, selected crystals of fluorapatite from series AP30 and AP40 experiments have been examined by single-crystal XRD methods as part of our previous EPR and X-ray structural analyses (Chen et al., 2002a; Pan et al., 2002b).

Selected crystals of fluorapatite and CaF_2-rich glasses were

mounted in Pyrex plugs and polished for electron microprobe analysis (EMPA) on a JEOL JXA-8600 Superprobe, equipped with three automatic wavelength-dispersive spectrometers (WDSs), one energy-dispersive spectrometer, and a cathodoluminescence (CL) detector, at the Department of Geological Sciences, U of SK. Operating conditions for quantitative EMPA analyses using WDS included an accelerating voltage of 10 kV, a beam current of 10 nA, a ~5-μm beam, and 30 s counting time. Also, the fluorapatite crystals and CaF_2-rich glasses from the Gd-rich runs (i.e., > 1500 ppm Gd) were analyzed by EMPA at 15 kV for Gd with a counting time of 90 s. Standards included a natural fluorapatite for Ca and P, synthetic phlogopite for F in fluorapatite and natural fluorite for F in CaF_2-rich glasses, and a synthetic $GdPO_4$ crystal for Gd. Gd concentration profiles across fluorapatite crystals in AP60-1 were made by EMPA traverses at 15 kV, 10 nA, ~ 1-μm beam, and 90 s counting time. Following Stormer et al. (1993), all EMPA analyses of fluorapatite were made on sections approximately parallel to the c-axis. A well-characterized Durango fluorapatite (Pan and Fleet, 1996; Young et al., 1969; Pan and Breaks, 1997) was also analyzed as an independent standard.

The Gd, Sr, and Mn contents of fluorapatite from AP30-0 and AP30-5 were determined on inclusion-free crystals using a Perkin-Elmer Sciex Elan 5000 inductively coupled plasma mass spectrometer (ICPMS), equipped with a CTEC UV laser system, at the Department of Geological Sciences, U of SK. Because of their large crystal sizes (~0.4 × 0.4× 3 mm), we used a laser beam of ~200 μm in diameter to maximize the signal-to-noise ratios. The fluorapatite crystals of series AP40 and AP50 were considerably smaller in size (up to ~300 μm in the maximum dimension) than those of series AP30 and were analyzed for trace elements by laser ablation-ICPMS (LA-ICPMS) on a Micromass hexapole instrument at the Department of Geological Sciences, U of SK, using a laser beam of ~50 to ~100 μm in diameter. Similarly, both fluorapatite crystals and CaF_2-rich glasses of AP60-3 and AP60-4 were analyzed in situ by LA-ICPMS on the Micromass instrument using a laser beam of ~20 μm in diameter. On both instruments, calcium was used as an internal standard to correct matrix effects and instrumental drifts, and NIST-612 glass was used for external calibration. Three to eight analyses were made for each sample to assess the homogeneity of trace elements. Also, a Durango fluorapatite was analyzed on both ICPMS instruments for comparison.

The REE, Sr, and Mn contents of the CaF_2-rich glasses from most experiments (including AP30-0, AP30-5, AP60-1, most of series AP40, and all of series AP50) were determined on the Micromass hexapole ICPMS, using the sample preparation procedure of Xie et al. (1994) and standard solution ICPMS analytical protocols of Jenner et al. (1990). The CaF_2-rich glasses were digested in HF-HNO_3 with or without addition of HCl. A comparison of analytical results and recommended values of REE in international reference materials and Durango fluorapatite showed that agreements for all REEs, Sr, and Mn are within 10%.

The Gd contents of the CaF_2-rich glasses from those AP30 experiments with > 1000 ppm Gd were determined by use of an energy-dispersive miniprobe multielement analyzer, i.e., X-ray fluorescence (XRF) microprobe, at the Department of Geological Sciences, U of SK. The instrumental design and operation of this XRF microprobe have been described in Cheburkin et al. (1997). In this study, a calibration curve for Gd was established based on the LA-ICPMS and EMPA results of three Gd-doped fluorapatite crystals (i.e., AP30-0, AP30-5, and AP30-1). XRF microprobe analyses of the CaF_2-rich glasses were made by placing them in sample holders made of 4-μm-thick Prolene films and using a counting time of 45 min. The accuracy and precision of the XRF microprobe have been evaluated by repeated analyses of Gd-bearing standard solutions and are shown to be within 5% for the range of Gd contents investigated in this study.

The wide range of REE concentrations investigated in this study required several analytical techniques (or same technique but on different instruments) to characterize the experimental products. Careful evaluation of the analytical results for selected reference materials and samples revealed no systematic differences among these techniques or instruments. For example, the results of XRF microprobe, EMPA, and LA-ICPMS analyses for the Gd concentration in a fluorapatite crystal from AP30-1 are within 8% of one another. Similarly, the Gd values for the CaF_2-rich glasses of AP30-1 and AP40-1 by XRF microprobe and solution ICPMS agree within 5%. The Gd, Sr, and Mn values for the CaF_2-rich glass of AP40-1 by LA-ICPMS and solution ICPMS are within 6%.

3. RESULTS AND DISCUSSION

3.1. Characterization of Experimental Products

All experimental products of this study consist of fluorapatite crystals and quenched CaF_2-rich glasses (Fig. 1a,b), except that AP40-0 with ~15 wt.% Gd_2O_3 in the starting material contains unreacted Gd_2O_3 as inclusions in both fluorapatite crystals and CaF_2-rich glass (Pan et al., 2002b). Fluorapatite of series AP30 experiments typically included several large prismatic crystals (up to 1 cm in length and ≥ 1 mm in diameter) that apparently grow on the wall of the Pt crucible, numerous intermediate grains (up to 2-mm long) at the bottom of the crucible, and minor amounts of small grains in CaF_2-rich glasses. Similarly, fluorapatite crystals from series AP40, AP50, and AP60 experiments are mostly concentrated at the bottom part of the Pt capsules, although minor amounts of small crystals also occur in the CaF_2-rich glasses (Fig. 1a,b). The crystal-glass ratios of all experiments are similar at ~1:3 (Fig. 1a,b).

Fluorapatite crystals in this study commonly contain elongated inclusions of CaF_2-rich glasses, which are almost invariably aligned parallel to the crystallographic c-axis (Chen et al., 2002a). Optical examination, as confirmed by single-crystal XRD analyses (Chen et al., 2002a; Pan et al., 2002b), revealed that the fluorapatite crystals of this study are not twinned. Also, sector zoning (cf. Rakovan and Reeder, 1996) was not observed. FTIR analyses did not detect any CO_3^{2-} or OH^- in fluorapatite of AP30-0 and AP30-1 (cf. Elliott, 1994; Santos and Clayton, 1995).

EMPA revealed that the fluorapatite crystals from all experiments are closely stoichiometric (Table 2), as expected for those synthesized from CaF_2-rich melts (Prener, 1967; Pan et al., 2002a, 2002b). Backscattered electron imaging and X-ray mapping showed that the distribution of Gd (and other REEs as well in series AP50 experiments) in the fluorapatite crystals is

Table 2. Representative major-element compositions of experimental products.

	Fluorapatite				CaF_2-rich glass			
Run#	AP30-1 $n = 12(\sigma)$	AP40-0 $n = 11(\sigma)$	AP50-1 $n = 12(\sigma)$	AP60-2 $n = 10(\sigma)$	AP30-1 $n = 12(\sigma)$	AP40-0 $n = 11(\sigma)$	AP50-1 $n = 12(\sigma)$	AP60-2 $n = 12(\sigma)$
P_2O_5(wt.%)	42.3 (5)	41.3 (5)	42.3 (4)	42.5 (3)	24.1 (8)	17.2 (6)	18.3 (7)	17.9 (8)
CaO	55.1 (3)	53.2 (5)	55.3 (4)	54.6 (3)	56.8 (9)	59.6 (7)	62.6 (5)	61.2 (6)
Gd_2O_3	1.2 (2)	2.9 (1)	0.01 (1)	1.11 (6)	2.3 (3)	5.3 (5)	0.01 (1)	2.3 (2)
F	3.7 (1)	3.53 (9)	3.71 (9)	3.62 (6)	26.9 (8)	29.4 (5)	30.3 (5)	30.1 (6)
O = −F	1.54	1.49	1.56	1.54	11.3	12.4	12.8	12.7
Total	100.7 (4)	99.5 (5)	99.8 (5)	100.3 (4)	98.8 (7)	99.1 (5)	98.4 (5)	98.8 (6)
P	6.00	6.00	6.00	6.00				
Ca	9.91	9.80	9.95	9.77				
Gd	0.06	0.17	0.00	0.06				
F	1.94	1.92	1.97	1.91				

Fluorapatite analyses for AP30-1 and AP40-0 are from Pan et al. (2002b). Chemical formula of fluorapatite are calculated to 6 P atoms.

generally homogeneous (Fig. 1c,d), as confirmed by quantitative EMPA and LA-ICPMS analyses (i.e., standard deviations of the Gd contents mostly $\leq 5\%$; Tables 2, 3, 4, and 5). The only exception is that the crystals of AP40-0 exhibit a minor variation (2.5–3.1 wt.% Gd_2O_3) from different grains. This is probably attributable to an incomplete homogenization of Gd in this Gd-rich run. Chen et al. (2002a) noted that the large fluorapatite crystals in series AP30 experiments are compositionally similar to the smaller grains. Similarly, the small fluorapatite grains in the CaF_2-rich glasses of series AP40, AP50, and AP60 experiments are compositionally indistinguishable from the larger crystals at the bottom of Pt capsules (Fig. 1a,b).

Powder XRD and FTIR analyses showed that the handpicked CaF_2-rich glasses for solution ICPMS analysis contain $\ll 5\%$ fluorapatite, hence insignificant contamination. Also, in situ EMPA and LA-ICPMS analyses of AP60-2, AP60-3, and AP60-4 did not detect any significant heterogeneity in either major or trace element composition of the CaF_2-rich glasses. The major element compositions of the CaF_2-rich glasses from series AP40, AP50, and AP60 experiments (Table 2) are invariably close to those expected from the phase relations of the pseudobinary CaF_2-$Ca_3(PO_4)_2$ system (cf. Prener, 1967). However, the CaF_2-rich glasses from series AP30 experiments are notably lower in Ca and F contents than their counterparts from experiments in sealed Pt capsules (Table 2), suggesting a possible loss of these two elements to volatilization in the former. EMPA showed that the CaF_2-rich glass of AP40-0 contains $\sim$5.3 wt.% Gd_2O_3 (Table 3), albeit imprecise owing to difficulties in the preparation of polished surfaces for this sample. This value is interpreted to represent the solubility of Gd_2O_3 in the phosphate-bearing CaF_2-rich melts.

Table 3. Results of Gd in series AP30 experiments.

Run #	Fluorapatite (ppm)	CaF_2-rich glass (ppm)	D (Gd)	$^{Ca2}Gd/^{Cal}Gd$
AP30-0	0.8 ± 0.1[a]	0.38[b]	2.1 (2)	0.13[e]
AP30-5	57 ± 4[a]	61[b]	0.93 (6)	0.20[f]
AP30-7	1100 ± 78[a]	1500[b]	0.73 (5)	
AP30-8	2,400 ± 160[d]	3,500 ± 130[c]	0.68 (4)	
AP30-9	3,500 ± 210[d]	5,500 ± 210[c]	0.64 (3)	
AP30-6	4,700 ± 240[d]	9,800 ± 320[c]	0.53 (2)	
AP30-1	10,000 ± 1,300[d]	21,000 ± 760[c]	0.49 (6)	1.4 (4)[g]

[a,b,c,d] represents analytical data from LA-ICPMS, solution ICPMS, XRF microprobe, and EMPA, respectively. Site-occupancy ratios ($^{Ca2}Gd/^{Cal}Gd$) are from single-crystal W-band EPR studies ([e], Pan et al., 2002a; [f], Chen et al., 2002b; and [g], Pan et al., 2002b). Uncertainties are one standard deviation.

3.2. Partitioning of Gd and Other REEs

Figure 2a shows that the partition coefficient of Gd [D(Gd)] between fluorapatite and CaF_2-rich melt from series AP30 experiments decreases with increasing Gd in fluorapatite from $\sim$2.0 at 0.8 ppm Gd before reaching a constant value of $\sim$0.5 at and above $\sim$5000 ppm Gd (Table 3). Similarly, D(Gd) from series AP40 experiments decreases from $\sim$2.0 to $\sim$0.5 with increasing Gd in fluorapatite but reaches the constant value at only $\sim$1000 ppm Gd (Fig. 2b, Table 4). These results show a pronounced non-Henry's Law behavior for the partitioning of Gd between fluorapatite and CaF_2-rich melt at low Gd concentrations. Although the magnitude of variations in the partition coefficients observed in this study is similar to those reported in

Table 4. Results of Gd in series AP40 and AP60 experiments.

Run Number	Fluorapatite	CaF_2-rich glass	D (Gd)
AP40-0	2.8 (2) wt.% Gd_2O_3[a]	$\sim$5.3 (5) wt.% Gd_2O_3[a]	0.53 (4)
AP40-1	1070 (49) ppm Gd[b]	2210 ppm Gd[c]	0.48 (2)
AP40-2	560 (32) ppm[b]	900 ppm[c]	0.62 (3)
AP40-3	225 (9) ppm[b]	260 ppm[c]	0.86 (3)
AP40-4	121 (7) ppm[b]	126 ppm[c]	0.96 (5)
AP40-5	66 (3) ppm[b]	66 ppm[c]	1.00 (4)
AP40-6	26.9 (9) ppm[b]	19 ppm[c]	1.42 (4)
AP40-7	7.0 (2) ppm[b]	3.54 ppm[c]	1.97 (5)
AP40-8	1.2 (2) wt.% Gd_2O_3[a]	2.3 (3) wt.% Gd_2O_3[a]	0.53 (3)
AP40-9	0.44 (9) wt.% Gd_2O_3[a]	0.8 (1) wt.% Gd_2O_3[a]	0.55 (4)
AP60-1	300 (200) ppm[a]	380 (25) ppm[b]	0.8 (5)
AP60-2	1.11 (6) wt.% Gd_2O_3[a]	2.3 (2) wt.% Gd_2O_3[a]	0.48 (1)
AP60-3	520 (12) ppm[b]	870 (20) ppm[b]	0.60 (2)
AP60-4	118 (8) ppm[b]	124 (9) ppm[b]	0.95 (6)

[a,b,c] represent analytical data from EMPA, LA-ICPMS, and solution ICPMS, respectively. Note that the surface Gd content of FAp in AP60-1 was extrapolated from the diffusion profile in Fig. 5. Uncertainties are one standard deviation.

Table 5. Results of REEs in series AP50 experiments.

	AP50-1			AP50-2			AP50-3			AP50-4		
	FAp (ppm)	Glass (ppm)	D (REE)	FAp (ppm)	Glass (ppm)	D (REE)	FAp (ppm)	Glass (ppm)	D (REE)	FAp (ppm)	Glass (ppm)	D (REE)
La	21.8 (4)	53	0.41	2.1 (2)	3.39	0.62	0.22 (3)	0.26	0.84	1050	2610	0.40
Nd	32.9 (7)	51	0.65	3.6 (2)	2.73	1.32	0.43 (8)	0.24	1.78	960	1820	0.53
Sm	35 (1)	52	0.67	3.75 (6)	3.02	1.24	0.35 (7)	0.22	1.59	1570	2290	0.69
Eu	30 (1)	50	0.60	3.4 (2)	2.93	1.16	0.42 (3)	0.25	1.68	2600	3830	0.68
Gd	37 (1)	55	0.67	4.9 (1)	4.01	1.22	0.81 (4)	0.47	1.71	570	870	0.65
Dy	34.3 (6)	58	0.59	3.9 (2)	3.79	1.03	0.46 (4)	0.32	1.44	1630	2420	0.67
Ho										2170	3150	0.68
Er	28 (1)	59	0.47	3.2 (3)	3.95	0.81	0.5 (1)	0.48	1.04	1420	2800	0.51
Tm										1610	3190	0.51
Yb	23 (1)	64	0.36	2.6 (1)	4.64	0.56	0.30 (8)	0.41	0.73	530	1640	0.32

REE contents of fluorapatite (FAp) by LA-ICPMS, those of CaF_2-rich glasses by solution ICPMS. Uncertainties in parentheses are one standard deviation.

the literature (e.g., Mysen, 1978; Harrison and Wood, 1980; Harrison, 1981), the upper limits of the non-Henry's Law behavior observed in the CaF_2-rich melts of this study are significantly higher than those reported for other minerals in silicate-melt systems (e.g., Mysen, 1978; Harrison and Wood, 1980; Harrison, 1981).

Watson and Green (1981) showed that D(REEs) between fluorapatite and silicate melts, with 0.4 to 3.2 wt.% total rare-earth oxides in the bulk composition, are independent of composition. The experiments of Watson and Green (1981) included excess F and were performed in sealed capsules, hence similar to those of series AP40. The REE contents of fluorapatite in Watson and Green (1981) are above the upper limit of non-Henry's Law partitioning observed in series AP40 experiments. It is noteworthy that experimentally measured D(REEs) in Fleet and Pan (1997) decrease with increasing REE contents from series B and D to series A and E, also a possible non-Henry's Law behavior.

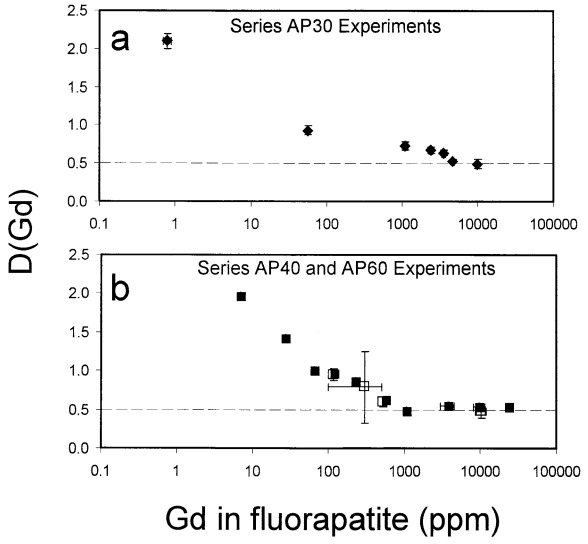

Fig. 2. Plots of D(Gd) as a function of the Gd concentration in fluorapatite from (a) series AP30 and (b) series AP40 (solid squares) and AP60 (open squares) experiments. Note that series AP30 and AP40 reach a similar constant D(Gd) value of ~0.5 but at different Gd concentrations (~5000 and ~1000 ppm, respectively) in fluorapatite. Error bars are one standard deviation; where not shown, error bars are smaller than the symbols.

The D(Gd) values of the present study are lower than those reported from previous experimental studies on silicate melts (Watson and Green, 1981) and hydrous phosphate-fluoride melts (Fleet and Pan, 1997) but are within the range obtained from natural apatites, whereby D(REEs) are known to vary by more than 2 orders of magnitude (Fleet and Pan, 1997). Pan and Fleet (2002) showed that D(REEs) are controlled by both intrinsic (crystal-chemical) and external (pressure-temperature-composition) factors (see also Watson and Green, 1981; Fleet and Pan, 1997). Therefore, a direct comparison between the results of the present study and those of previous experimental studies is difficult owing to differences in (1) melt compositions, (2) substitution mechanisms, and (3) pressure-temperature conditions. Pan et al. (2002b) noted that 2.8(3) wt.% Gd_2O_3 in fluorapatite of AP40-0 is significantly lower than that (10.4(5) wt.%) of another fluorapatite from a hydrothermal synthesis, despite having similar Gd_2O_3 contents in their starting materials (Fleet and Pan, 1995), and attributed this discrepancy to the presence of charge-compensating ions, Na^+ and Si^{4+}, for promoting the incorporation of Gd into the Ca sites in the latter experiment. Similarly, the absence of any charge-compensating cations in the experiments of the present study is most likely a major contributing factor to the low D(REEs) values (Tables 2, 3, and 4). Kovalenko et al. (1982) also noted that D(REEs) decrease with increasing equilibrium temperature. Therefore, the high temperature of experiments is another possible contributing factor to the low D(REEs) values of the present study.

Figure 3 shows that D(REEs) from series AP50 experiments vary systematically with atomic number. The most salient feature of these REE patterns is the convex-upward shape with maxima between Nd and Gd, similar to those observed in previous experiments and in nature (Watson and Green, 1981; Kovalenko et al., 1982; Ayers and Watson, 1993; Fleet and Pan, 1997). Also, the uptake of La in any composition is appreciably greater than that of Yb, with D(La)/D(Yb) ranging from 1.11 to 1.25 (see also Fleet and Pan, 1997). There are no

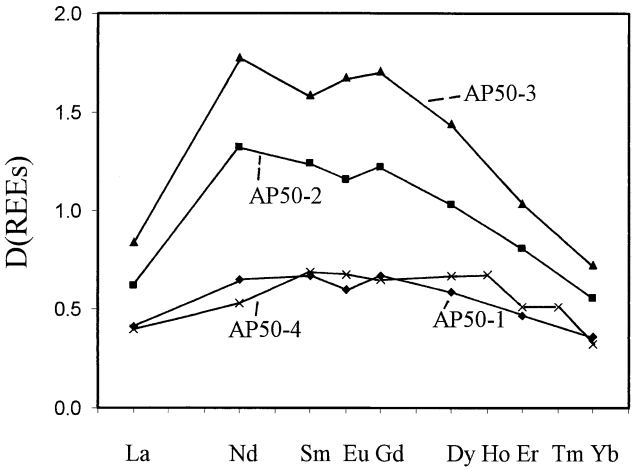

Fig. 3. Plots of D(REEs) as a function of atomic number for series AP50 experiments. Note that AP50-2 and AP30-3 with low total REE contents have more pronounced enrichments in middle REEs than AP50-1 and A P50-4.

significant Eu anomalies in series AP50 experiments. Therefore, Eu in our experiments behaves similarly to its neighboring trivalent REEs and most likely occurs mainly as Eu^{3+}, although oxygen fugacity was not controlled here.

The partition coefficients of individual REEs from series AP50 experiments (Table 5) similar to those from series AP30 and AP40 (Fig. 1), decrease with increasing total REEs in fluorapatite (Fig. 2), further supporting a non-Henry's Law behavior. Moreover, the D(Nd)/D(La) and D(Nd)/D(Yb) values (1.33–2.13 and 1.66–2.44, respectively) increase systematically with decreasing REE in fluorapatite, signifying a decrease in REE fractionation with increasing total REE concentration.

3.3. Partitioning of Sr and Mn

Strontium and Mn, both of which apparently originated from impurities in the starting materials, have also been analyzed in fluorapatite crystals and CaF_2-rich glasses for most experiments (Table 6) and are included for discussion for the following two reasons: (1) Sr is a close analog of Eu^{2+} because they have the same charge and similar ionic radii (Shannon, 1976; Watson and Green, 1981; Ayers and Watson, 1993) and (2) Mn, which has been shown to occur as Mn^{2+} by EPR (Pan et al., 2002a), provides an opportunity for examining the Henry's Law behavior of trace element partitioning involving isovalent-cation substitution at extremely low concentrations (Table 6).

LA-ICPMS analyses showed that Sr is homogeneously distributed in all fluorapatite crystals examined in this study (Table 6), at least on the scales of LA-ICPMS analysis (i.e., ~200 μm in AP30, ~50 to ~100 μm in AP40 and AP50, and ~20 μm in AP60-3 and AP60-4). Figure 4a shows that there is a positive correlation between Sr in fluorapatite and Sr in the CaF_2-rich glasses (R = 0.88, excluding samples AP30-0 and AP30-5), yielding a D(Sr) value of 1.4(1) (Table 6). This D(Sr) value, within the range (1.1–2.4) reported by Watson and Green (1981) for fluorapatite in equilibrium with silicate melts, supports the observation of Watson and Green (1981) that D(Sr) is insensitive to temperature, pressure, or melt composition within the limited range of silicate melt compositions that they studied (see also Ayers and Watson, 1993). Similarly, AP30-0 yields a D(Sr) of 1.08(8), which is close to that from series AP40, AP50, and AP60 experiments (Fig. 4a). However, the Sr contents of fluorapatite and CaF_2-rich glass from AP30-5 give an anomalously low D(Sr) value of 0.59(5) (Table 6).

The distribution of Mn in fluorapatite in our experiments, except for that of AP40-5, is also homogeneous on the scales of LA-ICPMS analysis (Table 6). There is a positive correlation

Table 6. Sr and Mn in fluorapatite and CaF_2-rich glasses and corresponding partition coefficients.

	Sr			Mn		
Run#	FAp (ppm)	Glass (ppm)	D (Sr)	FAp (ppm)	Glass (ppm)	D (Mn)
AP30-0	330 (26)	306	1.08 (8)	0.9 (2)	7.36	0.12 (3)
AP30-5	240 (13)	407		3.0 (4)	12.6	0.24 (3)
AP40-0	570 (28)	367	1.55 (8)	0.7 (2)	4.72	0.15 (4)
AP40-1	630 (18)	448	1.41 (4)	1.3 (6)	5.51	0.2 (1)
AP40-2	620 (14)	479	1.29 (3)	1.4 (9)	7.54	0.2 (1)
AP40-3	634 (3)	478	1.33 (1)	2.4 (4)	11.4	0.21 (4)
AP40-4	640 (10)	482	1.33 (2)	0.84 (7)	5.94	0.14 (1)
AP40-5	620 (10)	424	1.46 (2)	6 (7)	6.28	
AP40-6	640 (18)	501	1.28 (4)	1.5 (6)	21.6	
AP40-7	630 (10)	442	1.43 (2)	1.0 (1)	5.02	0.20 (2)
AP40-8	432 (4)	356 (11)	1.2 (1)	5.1 (6)	35 (2)	0.15 (2)
AP40-9	541 (5)	398 (12)	1.36 (8)	4.6 (8)	28 (2)	0.16 (3)
AP50-1	616 (3)	444	1.39 (1)	12 (1)	76	0.16 (1)
AP50-2	619 (5)	452	1.37 (1)	9 (2)	60	0.15 (3)
AP50-3	616 (8)	475	1.30 (2)	6 (1)	41	0.15 (2)
AP60-3	610 (12)	448 (7)	1.36 (8)	1.5 (3)	9.4 (9)	0.16 (3)
AP60-4	638 (9)	462 (9)	1.38 (8)	1.8 (4)	12 (1)	0.15 (3)
Average			1.4 (1)†			0.15 (1)‡

Sr and Mn in fluorapatite (FAp) of all experiments and those in the CaF_2-rich glasses of AP40-8, AP40-9, AP60-3, and AP60-4 were determined by LA-ICPMS; Sr and Mn in the CaF_2-rich glasses of other experiments by solution ICPMS; uncertainties are one standard deviation † from linear regression of all data except for those of AP30-0, AP30-5, and AP40-0; ‡ from linear regression of all data except for those of AP40-5 and AP40-6.

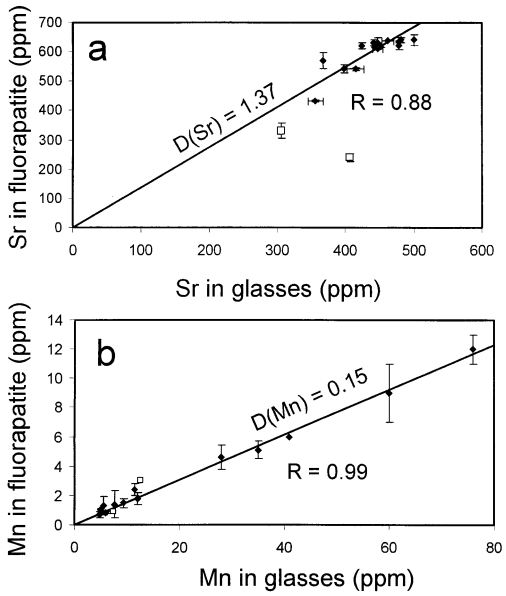

Fig. 4. Plots of (a) Sr in fluorapatite vs. Sr in CaF_2-rich glasses and (b) Mn in fluorapatite vs. Mn in CaF_2-rich glasses from series AP30, AP40, AP50, and AP60 experiments (AP40-5 and AP40-6 not shown). Lines are calculated from linear regression analyses (excluding AP30-0, AP30-5, and AP40-0 in a). R is correlation coefficient. Error bars are one standard deviation; where not shown, error bars are smaller than the symbols.

between Mn in fluorapatite and Mn in the CaF_2-rich glasses (R = 0.99, Fig. 4b), yielding a D(Mn) value of 0.15(1) (Table 6). The LA-ICPMS analysis of one fluorapatite crystal from AP40-5 yielded an anomalously high Mn content of 14.6 ppm, but those of two other crystals (2.59 and 1.43 ppm) from this experiment gave an average D(Mn) value of 0.3(1), which is close to those obtained from the other experiments (Table 6). Therefore, the partitioning of Mn^{2+} between fluorapatite and melt, different from those of trivalent REEs, obeys Henry's Law in the concentration range of this study (i.e., 0.9–12 ppm, Table 6).

3.4. Attainment of Equilibrium

The similarities of the experimental products (e.g., the fluorapatite-glass ratio and the major-element composition of the CaF_2-rich glasses; Fig. 1a,b, Table 2) to those expected from the phase relations of the pseudobinary CaF_2-$Ca_3(PO_4)_2$ system (cf. Prener, 1967) suggest that equilibrium was attained in our experiments. This suggestion is supported by the homogeneous compositions of the fluorapatite crystals and the CaF_2-rich glasses and is confirmed by the results of series AP60 experiments.

Prismatic fluorapatite crystals in AP60-1 are well preserved, indicating that dissolution and reprecipitation were minimal in this experiment. EMPA traverses reveal that the fluorapatite crystals in this experiment all contain a ~4.5-μm-wide Gd-depleted margin (Fig. 5). This apparent diffusion profile has been fitted with the equation of Crank (1975):

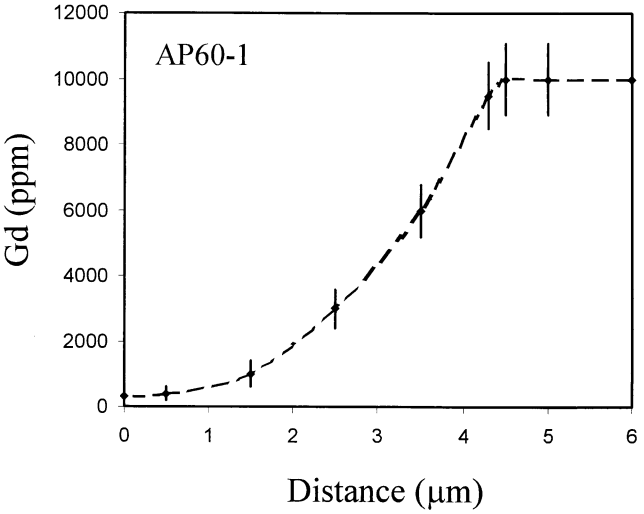

Fig. 5. Gd concentration profile across the margin of a fluorapatite crystal from AP60-1. This profile represents an average of six traverses across one fluorapatite grain. Error bars are one standard deviation. Note that the surface Gd concentration, which could not be analyzed directly by EMPA, was extrapolated from the trend.

$$C_{(x,t)} = C_i erf\left(\frac{x}{2\sqrt{Dt}}\right) \quad (0)$$

where $C_{(x,\,t)}$ is the Gd concentration at distance x and time t, C_i is the initial concentration, and D is the diffusion coefficient. Although the EMPA Gd contents in the Gd-depleted margin have significant uncertainties (Fig. 5), the magnitude of the diffusion coefficient D_{Gd} is largely controlled by the width of the margin. Indeed, the calculated D_{Gd} value of 3.4×10^{-18} m^2/s at 1220 °C is similar to D_{Dy} (1.2×10^{-18} m^2/s) and D_{Sm} (5.2×10^{-18} m^2/s) at this temperature, calculated from the Arrhenius equations of Cherniak (2000) and Watson et al. (1985), respectively. Also, the Gd concentration of 300 ± 200 ppm at the surface of the fluorapatite crystals, extrapolated from the diffusion profile (Fig. 5), and the Gd concentration of the CaF_2-rich glass by LA-ICPMS yield a D(Gd) value of 0.8(5) (Table 4). This value, albeit having a large uncertainty, is similar to that (0.86) from AP40-3 with a comparable Gd content in fluorapatite (Table 3). Moreover, D(Gd) from experiments AP60-2, AP60-3, and AP60-4 are within analytical uncertainties to those from AP40-8, AP40-2, and AP40-4, respectively (Fig. 2b). Similarly, D(Sr) and D(Mn) from experiments AP60-3 and AP60-4 are similar to those from experiments AP40-2 and AP40-4, respectively (Table 6), hence successful reversal experiments.

3.5. Origin of "the Henry's Law Problem" and Associated Inter-REE Fractionation

Thermodynamic analyses by previous investigators (Harrison and Wood, 1980; Harrison, 1981; Morlotti and Ottonello, 1982) suggested that the non-Henry's Law behavior of trace element partitioning in silicate systems is most likely related to vacancies in minerals. For example, Harrison and Wood (1980) suggested that the substitution of REE^{3+} ions for divalent

cations in the dodecahedral site of the garnet-group minerals at low concentrations is most likely charge-compensated by vacancies and can be expressed by the following exchange reaction:

$$\underset{\text{liquid}}{2REEO_{1.5}} + \underset{\text{garnet}}{3Mg^{2+}} \Leftrightarrow \underset{\text{liquid}}{3MgO} + \underset{\text{garnet}}{2REE^{3+}} + \underset{\text{garnet.}}{V_{Mg}} \quad (1)$$

Harrison and wood (1980) obtained the following relation:

$$D(REEs) \propto (1/V_{Mg})^{1/2} \quad (2)$$

Therefore, D(REEs) decrease with increase in the vacancy concentration at the dodecahedral site.

The incorporation of REE^{3+} in fluorapatite is complicated by the fact that these cations substitute for two stereochemically distinct Ca sites (i.e., nine-coordinated Ca1 and seven-coordinated Ca2) in this mineral (Hughes et al., 1991; Fleet and Pan, 1995; Gaft et al., 1997; Chen et al., 2002a, 2002b; Pan et al., 2002b). Single-crystal EPR studies (Chen et al., 2002a, 2002b) have demonstrated that the substitution mechanisms for the incorporation of Gd^{3+} (as a representative of trivalent REE ions) into the Ca1 and Ca2 sites in the synthetic fluorapatite of the present study are, respectively,

$$Ca1: 3Ca^{2+} \Leftrightarrow 2Gd^{3+} + \square \quad (3)$$

and

$$Ca2: Ca^{2+} + F^{-} \Leftrightarrow Gd^{3+} + O^{2-} \quad (4)$$

where $\square$ represents a Ca^{2+} vacancy. Moreover, Chen et al. (2002b) noted that the Gd^{3+} center at the Ca1 site has a highly triclinic local symmetry different from the uniaxial symmetry of the ideal Ca1 site in pure fluorapatite. This local symmetry reduction and the calculated direction of polyhedral distortion indicate that the Ca^{2+} vacancy is located at the next-nearest-neighbor Ca2 site in the c-axis channels, resulting in a Gd^{3+}--$\square$---Gd^{3+} arrangement, with the Gd^{3+} cations well separated (Chen et al., 2002b). Therefore, this is direct evidence for the involvement of Ca^{2+} vacancies in the incorporation of Gd^{3+} into the Ca1 site.

Following Harrison and Wood (1980), Eqn. 3 and 4 can be rewritten as exchange reactions between fluorapatite (FAp) and coexisting melts:

$$Ca1: \underset{\text{melt}}{2REEO_{1.5}} + \underset{\text{FAp}}{3Ca^{2+}} \Leftrightarrow \underset{\text{melt}}{3CaO} + \underset{\text{FAp}}{2REE^{3+}} + \underset{\text{FAp}}{V_{Ca2}} \quad (5)$$

and

$$Ca2: \underset{\text{melt}}{2REEO_{1.5}} + \underset{\text{FAp}}{2Ca^{2+}} + \underset{\text{FAp}}{2F^{-}} \Leftrightarrow \underset{\text{melt}}{CaO} + \underset{\text{melt}}{CaF_2} + \underset{\text{FAp}}{2REE^{3+}} + \underset{\text{FAp}}{2O^{2-}} \quad (6)$$

Therefore, the partition coefficients of REEs between fluorapatite and melt can be evaluated by independent incorporation of these elements into the Ca1 and Ca2 sites. Following Harrison and Wood (1980) again, we obtain "partial partition coefficients" at the Ca1 and Ca2 sites, respectively:

$$D(REE)_{Cal} \propto (1/V_{Ca2})^{1/2} \quad (7)$$

and

$$D(REE)_{Ca2} \propto PO_2 \quad (8)$$

where PO_2 is partial pressure of O_2. Therefore, the incorporation of REEs at the Ca1 site is inversely proportional to the abundance of Ca^{2+} vacancies at the Ca2 site in the c-axis channels, but the incorporation of REEs at the Ca2 site is independent of vacancies. Obviously, readily available Ca^{2+} vacancies would promote a preferential incorporation of REEs into the Ca1 site, whereas absence or saturation of vacancies would inhibit Eqn. 5, resulting in a preference of REEs for the Ca2 site. This is consistent with available data on the site-occupancy ratios of Gd in fluorapatite from single-crystal EPR studies and X-ray structure refinements (Hughes et al., 1991; Fleet and Pan, 1995; Chen et al., 2002b; Pan et al., 2002a, 2002b). For example, Pan et al. (2002b) noted that the Gd site-occupancy ratios ($^{Ca2}Gd/^{Ca1}Gd$) in fluorapatite decrease systematically with decreasing Gd content, changing from a preference for the Ca2 site in Gd-rich fluorapatite (Hughes et al., 1991; Fleet and Pan, 1995) to a marked preference for the Ca1 site in fluorapatite with ppm- to subppm-level Gd (Chen et al., 2002b). This marked preference of Gd for the Ca1 site in Gd-poor fluorapatite is apparently promoted by the availability of intrinsic Ca^{2+} vacancies in the c-axis channels at ppm concentrations. These point defects are unlikely to reach appreciable weight-percent concentrations in fluorapatite crystals synthesized from CaF_2-rich melts and hence the normal preference of Gd for the Ca2 site in Gd-rich fluorapatite (Pan et al., 2002b).

A control of the non-Henry's Law REE partitioning between fluorapatite and melt by intrinsic Ca^{2+} vacancies in the c-axis channels is also supported by the increase in the upper Gd limit from ~1000 ppm in series AP40 to ~5000 ppm in series AP30 (Fig. 2). This increase is readily explained by a larger amount of intrinsic Ca^{2+} vacancies in crystals from the latter experiments in Pt crucibles, owing to the apparent loss of CaF_2 to volatilization (Table 2). Such vacancies are expected to be much lower in crystals from series AP40 experiments in sealed Pt capsules.

In addition, the significant changes in inter-REE fractionations observed in series AP50 experiments (Fig. 3) are attributable to differences in stereochemical environment of the two Ca sites in fluorapatite (Fleet and Pan, 1997). The mean Ca1-O and Ca2-O distances in endmember fluorapatite (Hughes et al., 1989) are 2.554 and 2.463 Å, respectively. Amongst REE^{3+} ions, Nd would fit most readily in Ca1 of fluorapatite and Ce-Pr most readily in Ca2 of fluorapatite. Recognizing the marked preference of REEs for the Ca1 site at ppm- and subppm-level concentrations (Pan et al., 2002b), minimization of local strain at Ca1 and Ca2 is an adequate explanation for the characteristic convex-upward REE patterns with maxima at or close to Nd in fluorapatite (Fleet and Pan, 1997; Fig. 3) Moreover, mismatches in the ionic radii of REE^{3+} relative to the effective sizes of Ca^{2+} increase from Ca2 to Ca1 for La^{3+} but reversed for Yb^{3+} (Shannon, 1976). Therefore, the observed increase in D(La)/D(Nd) and D(Nd)/D(Yb) from AP50-1 to AP50-3 (Fig. 3) is consistent with an increased preference of REE^{3+} for the Ca1 site, as the total REE content in fluorapatite decreases.

3.6. Implications for Natural Apatites

Numerous previous studies have evaluated the roles of apatites in REE geochemical models for mantle compositions, crustal anatexis, magma evolution, and metamorphic/hydrothermal crystallization (e.g., Watson and Capobianco, 1981; Kovalenko et al., 1982; Pan and Fleet, 1996; Pan and Breaks, 1997; Dymek and Owen, 2001; Harlov and Föster, 2002), but all of them were based on the assumption of a Henry's Law behavior of REE partitioning. The D(REEs) from the present study obviously cannot be applied directly to geochemical modeling of silicate magmas or metamorphic/hydrothermal systems because of differences in melt/fluid compositions. Nevertheless, the convex-upward patterns of D(REEs) (Fig. 3) are similar to those observed in other systems (e.g., silicate melts: Watson and Green, 1981; Kovalenko et al., 1982; aqueous solutions: Ayers and Watson, 1993), suggesting a significant crystal-chemical control on the uptake of REEs by fluorapatite (Pan and Fleet, 2002). Moreover, we have shown above that the non-Henry's Law behavior of REE partitioning between fluorapatite and CaF_2-rich melts is largely controlled by intrinsic Ca^{2+} vacancies in this mineral. Therefore, the non-Henry's Law behavior of REE partitioning most likely occurs in other systems with low REE concentrations and should exert important controls on the REE systematics in those systems when apatite is present.

For example, Harrison (1981) evaluated the effects of the non-Henry's Law behavior of REE partitioning between garnet-group minerals and silicate melts in the origin of basaltic magmas. Her calculations showed that significant variations can occur in the absolute REE contents of melts derived from a garnet lherzolite if non-Henry's Law partition coefficients are used for garnet. Similar variations in REE contents are expected during melting processes (e.g., crustal anatexis for the generation of granites: Watson and Capobianco, 1981) involving fluorapatite if non-Henry's Law D(REEs) are encountered. Harrison (1981) also noted that the non-Henry's Law behavior extends over a wider concentration range for HREEs (e.g., Tm) than for LREEs (e.g., Ce). For a given total REE concentration in garnet, it is possible that LREEs have Henry's Law D(REEs), whereas HREEs may still deviate from Henry's Law. As a result, the LREE/HREE values in garnet and coexisting melts are expected to change as the total REE content in garnet varies. Although our study did not investigate the possible difference in the range of non-Henry's Law behavior among different REEs, a systematic variation in D(REEs) between fluorapatite and CaF_2-rich melts with atomic number is evident in Figure 3. The variation here, however, is readily attributable to differential substitutions of REEs into the two distinct Ca sites in this mineral (see discussion above).

Figure 6 illustrates the effects of a non-Henry's Law behavior of REE partitioning on the REE characteristics of rhyolites derived from fractional crystallization of an andesitic parental melt. Following Watson and Capobianco (1981), we took the average Circum-Pacific andesite of Taylor (1969) as the parental melt and assumed a crystallization/removal of 55% plagioclase, 20% hornblende, 5% augite, and 0.89% fluorapatite. Here, we multiplied D(REEs) from AP50-4, representing a Henry's Law behavior, by 100 to bring them close to those observed in silicate magmatic systems (e.g., Watson and Green, 1981; Kovalenko et al., 1982). Also, we took D(REEs) from AP50-3 to represent the non-Henry's Law behavior and multiplied them by 100 times (i.e., assuming a similar magnitude of difference between Henry's Law and non-Henry's Law D(REEs) in silicate magmatic systems). Figure 6 shows that Henry's Law and non-Henry's Law D(REEs) of fluorapatite result in significant differences in both the absolute REE concentration and the REE fractionation in the residual rhyolitic melts.

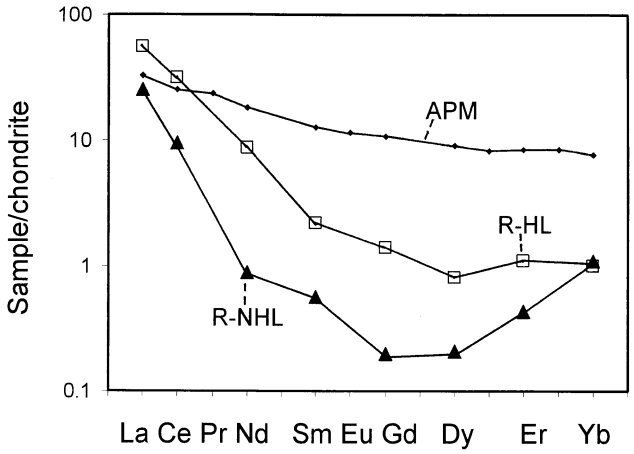

Fig. 6. Comparison of the effects of Henry's Law and non-Henry's Law D(REEs) on the fractional crystallization for the formation of rhyolites from an andesitic parental melt (cf. Watson and Capobianco, 1981). D(REEs) for plagioclase and hornblende are from Arth and Barker (1976) and those for augite from Nagasawa and Schnetzler (1971), except that D(La) values are extrapolated. Note that Henry's Law and non-Henry's Law D(REEs) from AP50-4 and AP50-3, respectively, have been multiplied by 100 to account for differences in melt compositions and P-T conditions. Also, D(Ce) values for fluorapatite are extrapolated, and Eu is not included in modeling.

In addition, Watson and Green (1981) noted that D(Sr), and by analog D(Eu^{2+}), is significantly lower than D(REE^{3+}) (see also Ayers and Watson, 1993). Therefore, crystallization of fluorapatite from a silicate melt without any Eu anomaly would result in a positive Eu anomaly in the residual melt. In the present study, however, D(Sr) is higher than D(Gd^{3+}) at most REE concentrations in fluorapatite, except for REE concentrations at or near subppm-level where D(REEs) are significantly higher owing to the non-Henry's Law behavior. This variation in relationship between D(Sr) and D(REE^{3+}) is also expected in natural apatites because of the complex dependence of D(REE^{3+}) on both intrinsic and external factors (Pan and Fleet, 2002) and the relative insensitivity of D(Sr) to P-T-X conditions (Watson and Green, 1981; this study). Therefore, care must be taken in interpreting Eu anomalies in natural apatites.

The most important implication of the observed non-Henry's Law REE partitioning and its association with intrinsic Ca^{2+} vacancies is perhaps for the uptake of REEs by biogenic apatites, which are characterized by nonstoichiometry (Elliott, 1994; Wilson et al., 1999 and references therein). In recent years, REE compositions and Sm-Nd isotopes in biogenic apatite (i.e., a major component of bones, teeth, and fossils of vertebrates) have been increasingly used for paleoenvironmental reconstruction because they are thought to closely reflect the REE compositions of ancient seawater or surrounding sediment

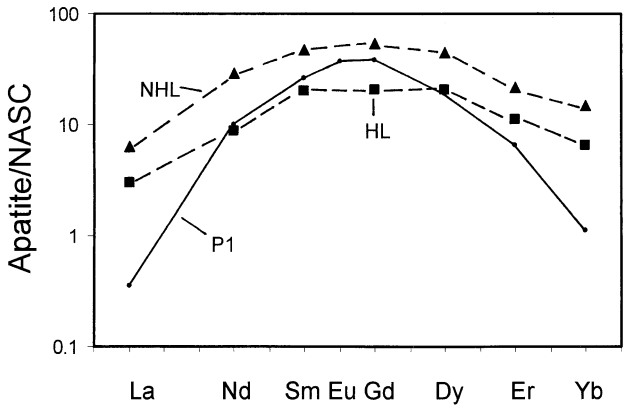

Fig. 7. Comparison of calculated REE patterns of apatite (dashed lines), assuming equilibrium with seawater (DeBaar et al., 1985), and that of representative biogenic apatite (solid line: P1 of Grandjean and Albaréde, 1989) normalized to the North American Shale Composite (NASC; Gromet et al., 1984). The Henry's Law (HL) and non-Henry's Law (NHL) REE patterns are calculated using D(REEs) of AP50-4 and AP50-3, respectively. Similar to Reynard et al. (1999), enrichment factors with respect to seawater of $\sim 10^7$ have been used to reproduce the middle REEs of biogenic apatite. Note that non-Henry's Law D(REEs) result in a more marked enrichment between Sm and Gd than Henry's Law D(REEs), which is a characteristic feature of ancient biogenic apatite (e.g., Wright et al., 1984; Grandjean and Albaréde, 1989; Grandjean-Lécuyer et al., 1993).

pore fluids (Wright et al., 1984; Toyoda and Tokonami, 1990; Grandjean-Lëcuyer et al., 1993; Holmden et al., 1997; Reynard et al., 1999). The observed non-Henry's Law behavior for non-stoichiometric fluorapatite at high temperatures, if it can be extrapolated to ambient temperatures, would exert significant controls on the uptake of REEs by biogenic apatite. For example, it has been discussed above that Eu anomalies in fossil biogenic apatite, commonly used as a redox indicator, must be interpreted with caution. Also, significant variations in inter-REE fractionation are expected during the trapping of these elements into biogenic apatite from seawater or pore fluids, because D(REEs), D(Nd)/D(La), and D(Nd)/D(Yb) all change with progressive reduction in the availability of intrinsic Ca^{2+} vacancies in the c-axis channels. For example, the variation in REE patterns of fossil biogenic apatite from Cambrian to post-Cretaceous time was originally interpreted to record a secular change in seawater composition (e.g., Wright et al., 1984; Grandjean-Lëcuyer et al., 1993). Reynard et al. (1999) showed that the bell-shaped REE patterns, observed commonly in Lower Paleozoic conodonts, are related to small degrees of recrystallization of biogenic apatite and, therefore, are controlled by fractionation of REEs between apatite and water. Our experimentally determined D(REEs) (Fig. 3) provide further support for such a crystal-chemical control. Figure 7 shows that the non-Henry's Law D(REEs) better predict the bell-shaped REE patterns of biogenic apatite than those from a Henry's Law behavior. Therefore, the non-Henry's Law behavior of REE partitioning between apatite and water is a possible contributing factor for the commonly observed, bell-shaped REE patterns in fossil biogenic apatite.

Acknowledgments—We thank J. C. Ayers, D. E. Harlov, and B. O. Mysen for incisive criticism and many helpful suggestions. We also thank T. Bonli (electron microprobe) and Q. Xie (ICPMS) for analytical assistance and the Natural Science and Engineering Research Council (NSERC) of Canada for financial support.

Associate editor: B. Mysen

REFERENCES

Arth J. G. and Barker F. (1976) Rare-earth partitioning between hornblende and dacitic liquid and implications for the genesis of trondhejmitic-tonalitic magmas. *Geology* **4,** 534–536.

Ayers J. C. and Watson E. B. (1993) Apatite/fluid partitioning of rare earth elements and strontium: Experimental results at 1.0 GPa and 1000 °C and application to models of fluid-rock interaction. *Chem. Geol.* **110,** 299–314.

Cheburkin A. K., Frei R., and Shotyk W. (1997) An energy-dispersive miniprobe multielement analyzer (EMMA) for direct analysis of trace elements and chemical age dating in single mineral grains. *Chem. Geol.* **135,** 75–87.

Chen N., Pan Y., and Weil J. A. (2002a) Electron paramagnetic resonance spectroscopic study of synthetic fluorapatite: Part I. Substitution mechanism and local structural environment of Gd at the Ca2 site. *Am. Mineral.* **87,** 37–46.

Chen N., Pan Y., Weil J. A., and Nilges M. J. (2002b) Electron paramagnetic resonance spectroscopic study of synthetic fluorapatite: Part II. Gd at the Ca1 site and association with vacancy at Ca2 site. *Am. Mineral.* **87,** 47–55.

Cherniak D. J. (2000) Rare earth element diffusion in apatite. *Geochim. Cosmochim. Acta* **64,** 3871–3885.

Crank J. (1975) *The Mathematics of Diffusion*, 2d ed. Oxford University Press, UK.

De Baar H. J. W., Bacon M. P., Drewer P. G., and Bruland K. W. (1985) Rare earth elements in the Pacific and Atlantic oceans. *Geochim. Cosmochim. Acta* **49,** 1943–1959.

Dymek R. F. and Owen B. E. (2001) Petrogenesis of apatite-rich rocks (nelsonites and oxide-apatite gabbronorites) associated with massif anorthosites. *Econ. Geol.* **96,** 797–815.

Elliott C. J. (1994) *Structure and Chemistry of the Apatites and Other Calcium Orthophosphates*. Elsevier, Amsterdam.

Fleet M. E. and Pan Y. (1995) Site preference of rare earth elements in fluorapatite. *Am. Mineral.* **80,** 329–335.

Fleet M. E. and Pan Y. (1997) Rare-earth elements in fluorapatite: Uptake from H_2O-bearing phosphate-fluoride melts and the role of volatile components. *Geochim. Cosmochim. Acta* **61,** 4745–4760.

Fleet M. E., Liu X., and Pan Y. (2000a) Rare-earth elements in chlorapatite $[Ca_{10}(PO_4)_6Cl_2]$: Uptake, site preference and degradation of monoclinic structure. *Am. Mineral.* **85,** 1437–1446.

Fleet M. E., Liu X., and Pan Y. (2000b) Site preference of rare-earth elements in hydroxyapatite $[Ca_{10}(PO_4)_6(OH)_2]$. *J. Solid State Chem.* **149,** 391–398.

Grandjean P. and Albaréde F. (1989) Ion probe measurements of rare earth elements in biogenic phosphates. *Geochim. Cosmochim. Acta* **53,** 3179–3183.

Grandjean-Lécuyer P., Feist R., and Albaréde F. (1993) Rare earth elements in old biogenic apatites. *Geochim. Cosmochim. Acta* **57,** 2507–2514.

Gromet L. P., Dymek R. F., Haskin L. A., and Korotev R. L. (1984) The North American Shale Composite: Its composition, major and trace element characteristics. *Geochim. Cosmochim. Acta* **48,** 2469–2482.

Harlov D. E. and Föster H.-J. (2002) High-grade fluid metasomatism on both a local and regional scale: The Seward Peninsula, Alaska and the Val Strona di Omegna, Ivrea-Verbano zone, northern Italy. Part II: Phosphate mineral chemistry. *J. Petrol.* **43,** 801–824.

Harlov D. E., Föster H.-J., and Nijland T. G. (2002) Fluid-induced nucleation of (Y+REE)-phosphate minerals within apatite: Nature and experiment. Part I. Chlorapatite. *Am. Mineral.* **87,** 245–261.

Harrison W. J. (1981) Partition coefficients for REE between garnets and liquids: Implications of non-Henry's Law behaviour for models of basalt origin and evolution. *Geochim. Cosmochim. Acta* **45,** 1529–1544.

Harrison W. J. and Wood B. J. (1980) Partitioning of REE between garnets and liquids: The role of defect equilibria. *Contrib. Mineral. Petr.* **72,** 145–155.

Holmden C., Creaser R. A., Muehlenbachs K., Leslie S. A., and Bergstrom S. M. (1997) Isotopic and elemental systematics of Sr and Nd in 454 Ma biogenic apatites: Implications for paleoseawater studies. *Earth Planet. Sci. Lett.* **142,** 425–437.

Hughes J. M., Cameron M., and Mariano A. N. (1991) Rare-earth-element ordering and structural variations in natural rare-earth-bearing apatites. *Am. Mineral.* **76,** 1165–1173.

Hughes J. M., Cameron M., and Crowley K. D. (1989) Structural variations in natural F, OH, and Cl apatites. *Am. Mineral.* **74,** 870–876.

Jenner G. A., Longerich H. P., Jackson S. E., and Fryer B. J. (1990) ICP-MS—a powerful tool for high-precision trace-element analysis in Earth Sciences: Evidence for analysis of selected U.S.G.S. reference samples. *Chem. Geol.* **83,** 133–148.

Kovalenko V. I., Antipin V. S., Vladykin N. V., Smirnova Y. V., and Balashov Y. A. (1982) Rare-earth distribution coefficients in apatite and behavior in magmatic processes. *Geochem. Int.* **19,** 174–183.

Mackie P. E. and Young R. A. (1973) Location of Na dopant in fluorapatite, $Ca_5(PO_4)_3F$:Nd. *J. App. Crystallogr.* **6,** 26–31.

Morlotti R. and Ottonello G. (1982) Solution of rare-earth elements in silicate solid phases: Henry's Law revisited in light of defect chemistry: Garnet, clinopyroxene and plagioclase. *Phys. Chem. Miner.* **8,** 87–97.

Mysen B. O. (1978) Limits of solution of trace elements in minerals according to Henry's Law: Review of experimental data. *Geochim. Cosmochim. Acta* **42,** 871–885.

Nagasawa H. and Schnetzler C. C. (1971) Partitioning of rare earth, alkali and alkaline earth elements between phenocrysts and acidic igneous magma. *Geochim. Cosmochim Acta* **25,** 953–968.

Navrotsky A. (1978) Thermodynamics of elements partitioning: 2-defect chemistry and "The Henry's Law Problem." *Geochim. Cosmochim. Acta* **42,** 887–902.

Pan Y. and Breaks F. W. (1997) Rare earth elements in fluorapatite, Separation Lake area, Ontario: Evidence for S-type granite–rare-element pegmatite linkage. *Can. Mineral.* **35,** 659–671.

Pan Y. and Fleet M. E. (1996) Rare earth element mobility during prograde granulite facies metamorphism: Significance of fluorine. *Contrib. Mineral. Petr.* **123,** 251–262.

Pan Y. and Fleet M. E. (2002) Compositions of the apatite-group minerals: Substitution mechanisms and controlling factors. *Rev. Mineral. Geochem.* **48,** 13–49.

Pan Y., Chen N., Weil J. A., and Nilges M. J. (2002a) Electron paramagnetic resonance spectroscopic study of synthetic fluorapatite: Part III. Structural characterization of sub-ppm-level Gd and Mn in minerals at W-band frequency. *Am. Mineral.* **87,** 1333–1341.

Pan Y., Fleet M. E., Chen N., Weil J. A., and Nilges M. J. (2002b) Site preference of Gd in synthetic fluorapatite by single-crystal W-band EPR and X-ray structure refinement: A comparative study. *Can. Mineral.* **40,** 1103–1112.

Prener J. S. (1967) The growth and crystallographic properties of calcium fluo- and chlorapatite crystals. *J. Electrochem. Soc.* **114,** 77–83.

Rakovan J. and Reeder R. J. (1996) Intracrystalline rare earth element distributions in apatite surface structural influences on incorporation during growth. *Geochim. Cosmochim. Acta* **60,** 4435–4445.

Reynard B., Lëcuyer C., and Grandjean P. (1999) Crystal-chemical controls on rare-earth element controls in fossil biogenic apatites and implications for paleoenvironmental reconstruction. *Chem. Geol.* **155,** 233–241.

Santos R. V. and Clayton R. N. (1995) The carbonate content in high-temperature apatite: An analytical method applied to apatite from the Jacupiranga alkaline complex. *Am. Mineral.* **80,** 336–344.

Shannon R. D. (1976) Revised effective ionic radii and systematic studies of interatomic distances in halides and chalcogenides. *Acta Crystallogr.* **A32,** 751–767.

Siemann M. G. and Schramm M. (2002) Henry's and non-Henry's law behavior of Br in simple marine systems. *Geochim. Cosmochim. Acta* **66,** 1387–1399.

Stormer J. C., Pierson M. L., and Tacker R. C. (1993) Variation of F and Cl X-ray intensity due to anisotropic diffusion in apatite during electron microprobe analysis. *Am. Mineral.* **78,** 641–648.

Taylor S. R. (1969) Trace element geochemistry of andesites and associated calc-alkaline rocks. In *Proceedings of Andesite Conference*, Eugene, Oregon, pp. 43–63.

Toyoda K. and Tokonami M. (1990) Diffusion of rare-earth elements in fish teeth from deep sea sediments. *Nature* **345,** 607–609.

Watson E. B. and Capobianco C. J. (1981) Phosphorus and the rare earth elements in granites: An assessment of the role of apatite. *Geochim. Cosmochim. Acta* **45,** 2349–2358.

Watson E. B. and Green T. H. (1981) Apatite/liquid partition coefficients for the rare earth elements and strontium. *Earth Planet. Sci. Lett.* **56,** 405–421.

Watson E. B., Harrison T. M., and Ryerson F. J. (1985) Diffusion of Sm, Sr and Pb in fluorapatite. *Geochim. Cosmochim. Acta* **45,** 2349–2358.

Wilson R. M., Elliott C. J., and Dowker S. E. P. (1999) Rietveld refinement of the crystallographic structure of human dental enamel apatites. *Am. Mineral.* **84,** 1406–1414.

Wright J., Seymour R. S., and Shaw H. (1984) REE and neodymium isotopes in conodont apatite: Variations with geological and depositional environment. *Geol. Soc. Am. Spec. Paper.* **196,** 325–340.

Xie Q., Jain J., Sun M., Kerrich R., and Fan J. (1994) Multi-element analysis of low abundance international reference material BIR-1: Results by ICP-MS. *Geostandard. Newslett.* **18,** 53–63.

Young E. J., Myers A. T., Munson E. L., and Conklin N. M. (1969) Mineralogy and geochemistry of fluorapatite from Cerro de Mercado, Durango, Mexico. *USGS Prof. Paper* 650-D, pp. 84–93.